Title

Thermonuclear neutron emission from a sheared-flow stabilized Z-pinch

Journal

Physics of Plasmas, 28(11)

ISSN

1070-664X

Authors

Mitrani, James M

Brown, Joshua A

Goldblum, Bethany L

et al.

Publication Date

2021-11-01

DOI

10.1063/5.0066257

Peer reviewed

LAWRENCE
LIVERMORE
NATIONAL
LABORATORY

LLNL-JRNL-831935

Thermonuclear neutron emission from a sheared-flow stabilized Z-pinch

J. M. Mitrani, J. A. Brown, B. L. Goldblum, T. A. Laplace, E. L. Claveau, Z. T. Draper, E. G. Forbes, R. P Golingo, H. S. McLean, B. A. Nelson, U. Shumlak, A. D. Stepanov, T. R. Weber, Y. Zhang, D. P. Higginson

February 21, 2022

Physics of Plasmas

Disclaimer

Thermonuclear neutron emission from a sheared-flow stabilized Z-pinch

James M Mitrani,[1, a)] Joshua A Brown,[2] Bethany L Goldblum,[2, 3] Thibault A Laplace,[2] Elliot L Claveau,[4, b)] Zack T Draper,[4, c)] Eleanor G Forbes,[4, d)] Ray P Golingo,[4, e)] Harry S McLean,[1] Brian A Nelson,[4, c)] Uri Shumlak,[4, f)] Anton Stepanov,[4, c)] Tobin R Weber,[4, c)] Yue Zhang,[4, g)] and Drew P Higginson[1]

[1)] *Lawrence Livermore National Laboratory, Livermore, CA, 94551*

[2)] *Department of Nuclear Engineering, University of California, Berkeley, CA, 94709*

[3)] *Nuclear Science Division, Lawrence Berkeley National Laboratory, Berkeley, CA, 94720*

[4)] *Aerospace and Energetics Research Program, University of Washington, Seattle, Washington 98195*

(Dated: 1 November 2021)

The Fusion Z-pinch Experiment (FuZE) is a sheared-flow stabilized Z-pinch designed to study the effects of flow stabilization on deuterium plasmas with densities and temperatures high enough to drive nuclear fusion reactions. Results from FuZE show high pinch currents and neutron emission durations thousands of times longer than instability growth times. While these results are consistent with thermonuclear neutron emission, energetically-resolved neutron measurements are a stronger constraint on the origin of the fusion production. This stems from the strong anisotropy in energy created in beam-target fusion, compared to the relatively isotropic emission in thermonuclear fusion. In dense Z-pinch plasmas, a potential and undesirable cause of beam-target fusion reactions is the presence of fast growing, "sausage" instabilities. This work introduces a new method for characterizing beam instabilities by recording individual neutron interactions in plastic scintillator detectors positioned at two different angles around the device chamber. Histograms of the pulse-integral spectra from the two locations are compared using detailed Monte Carlo simulations. These models infer the deuteron beam energy based on differences in the measured neutron spectra at the two angles, thereby discriminating beam-target from thermonuclear production. An analysis of neutron emission profiles from FuZE precludes the presence of deuteron beams with energies greater than 4.65 keV with a statistical uncertainty of 4.15 keV and a systematic uncertainty of 0.53 keV. This analysis demonstrates that axial, beam-target fusion reactions are not the dominant source of neutron emission from FuZE. These data are promising for scaling FuZE up to fusion reactor conditions.

[a)]mitrani1@llnl.gov

[b)]Now at MIT Plasma Science and Fusion Center, Cambridge, MA, 02139

[c)]Now at Zap Energy Inc, Seattle, WA, 91804

[d)]Now at Aerojet Rocketdyne, El Segundo, CA, 90245

[e)]Now at Fuse Energy Inc, Napierville, QC, J0J 1L0

[f)]Now co-affiliated with Zap Energy Inc, Seattle, WA, 91804

[g)]Now at Lam Research, Fremont, CA, 94538

I. INTRODUCTION

Designs for positive net-energy fusion reactors must satisfy the Lawson criterion[1], which states that hot and dense plasmas need be confined for long timescales. The Z-pinch is one of the simplest concepts for plasma confinement. It consists of axial current flowing between two electrodes, forming a cylindrical plasma volume. A static equilibrium for plasma confinement in Z-pinches is achieved when an inward $j_z \times B_\theta$ force is balanced with an outward pressure gradient, ∇p,

$$\frac{\mathrm{d}}{\mathrm{d}R}\left(p + \frac{B_\theta^2}{2\mu_0}\right) + \frac{B_\theta^2}{\mu_0 R} = 0, \tag{1}$$

where R is the radial coordinate, j_z is the axial current, B_θ is the azimuthal magnetic field, p is the plasma pressure, and μ_0 is the magnetic permeability in vacuum. If long confinement timescales can be maintained for Z-pinch plasmas, then increasing the pinch current will result in plasma densities and temperatures high enough for positive net energy fusion reactor conditions[2,3].

Although Z-pinch equilibria were discovered as early as 1934[4], subsequent theoretical and experimental results[5–8] demonstrated large-scale, fast-growing plasma instabilities. Two of the most virulent instabilities in Z-pinch plasmas are the m=0 "sausage" instability and the m=1 "kink" instability, where m is the azimuthal mode number. Fast-growing instabilities in Z-pinch plasmas lower plasma confinement timescales by disrupting current flow. To mitigate the destabilizing effects of the sausage and kink instabilities, fusion research devices have largely moved away from the linear Z-pinch design.

Theoretical[9] and experimental[2,10] results show that the application of radially-sheared, axial plasma flows can mitigate the growth of plasma instabilities in linear Z-pinch plasmas, resulting in plasma lifetimes significantly larger than instability growth times. Shumlak and Hartman[9] calculated that plasma flows with sub-Alfvenic flow velocities can stabilize Z-pinches against m=1 instabilities. Shumlak and Hartman's calculations do not assume the presence of a close-fitting conducting wall and are performed in a Kadomtsev equilibrium[11], which is marginally stable to m=0 instabilities. Subsequent measurements[12] in a first generation sheared-flow stabilized (SFS) Z-pinch device, demonstrated stabilization against m=1 instabilities in Z-pinch plasma columns. Z-pinch plasmas with pinch currents of up to ∼50 kA and plasma durations of up to ∼30 μs were observed.

The Fusion Z-pinch Experiment (FuZE) is a second generation SFS Z-pinch that is designed to study the effects of sheared-flow stabilization on Z-pinch plasmas in a fusion regime. FuZE uses a faster, higher-energy capacitor bank to deliver more power to the device chamber, resulting in Z-pinch plasmas with higher pinch currents (>200 kA), plasma densities ($\sim 10^{17}$ cm^{-3}), and ion temperatures ($\sim$1 keV). Plasma densities and temperatures are high enough to drive measurable fusion reactions when D_2 fill gas mixtures are injected into the device chamber.

To lowest order, fusion of two deuterons ("DD fusion") at rest will produce a neutron with a kinetic energy of 2.45 MeV and a ^{3}He ion with a kinetic energy of 0.82 MeV. Recent results[13,14] from FuZE show neutron production with yields of $\sim 10^5$ neutrons per discharge, long emission durations of ~ 5 μs, and neutron emission regions (33 cm length) comparable to the plasma volume (50 cm length). Neutron emission durations of 5 μs are >1000 times greater than instability growth times, and are therefore consistent with thermonuclear neutron production.

In Z-pinch plasmas, m=0 instabilities can result in electric-fields large enough to drive energetic ion beams into the plasma column. If a deuterium fill gas is used, this results in neutron emission through beam-target fusion reactions[15,16]. Due to the kinetics of the fusion reaction, neutron energies emitted from beam-target fusion reactions are significantly upshifted parallel to the beam direction and downshifted opposite the beam direction. Conversely, given the isotropic nature of a thermal Maxwellian plasma, neutron energies emitted from thermonuclear reactions are relatively spatially isotropic in the lab frame. To determine whether neutrons emitted from FuZE originate from thermonuclear or beam-target fusion reactions, relative neutron energies are inferred from detectors placed at multiple angular locations around the fusing plasma column along the direction of potential beam acceleration from m=0 instabilities.

A method for energetically-resolved neutron measurements is demonstrated for diagnosing neutron production from fusion plasmas with neutron emission durations longer than a microsecond. Neutron emission is measured with fast plastic, organic scintillators coupled to photomultiplier tubes (PMTs) operating in pulse counting mode. The PMT response is measured for the neutron emission duration of the fusing plasma. Individual pulses are integrated using a template fitting approach to calculate the light output observed for a single neutron event. The light output is proportional to the energy of the recoil proton

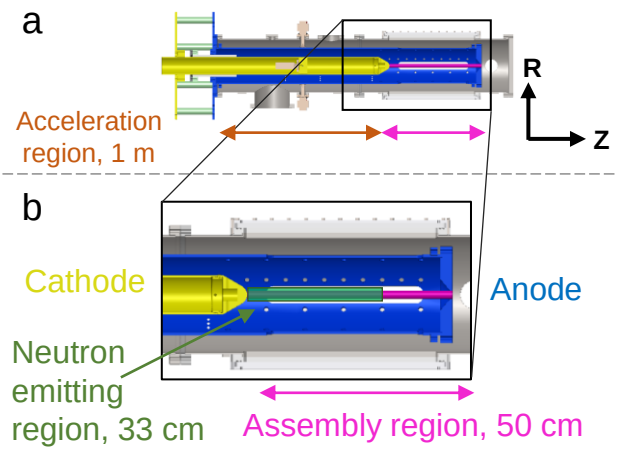

FIG. 1: (a) Drawing of FuZE device chamber. Neutral gas is injected and ionized in the 1 m long acceleration region. The ionized gas runs down the coaxial electrode arrangement and assembles into a Z-pinch plasma column in the 50 cm long assembly region. (b) Zoomed in view of the assembly region, showing the cathode tip and anode end wall. The length of the neutron emitting region (green) is 33 cm.[14].

from neutron interactions in the detection volume. Additionally, a collection of neutron interactions from a mono-energetic neutron flux has unique statistical distribution of recoil protons. The recoil proton distribution can be numerically modeled and allows inference between the measured pulses and the incident neutron energy. With several detectors placed around the fusing plasma, this detection methodology allows for a calculation of spatially-resolved neutron emission profiles.

This manuscript is organized as follows: Section (II) briefly describes operating details of the FuZE device and the neutron diagnostics suite. Section (III) provides the physical basis for neutron energy anisotropies from beam-target fusion reactions. Results from energetically-resolved neutron measurements on the FuZE device are described in Section (IV). A discussion of the results is presented in Section (V). Concluding remarks are given in Section (VI).

II. MATERIALS AND METHODS

A. The Fusion Z-pinch Experiment (FuZE)

Operating parameters and device specifications for FuZE are described previously[13,14,17]. A drawing of the FuZE chamber is shown in Figure (1). Helium fill gas mixtures with 20% D_2 by pressure are injected in an acceleration region between two cylindrical electrodes and ionized by an applied voltage. Voltage is supplied by a capacitor bank consisting of twelve, 830 μF capacitors. For the data presented in this manuscript, the capacitor bank is charged to -6 kV. In the acceleration region, neutral gas is injected, ionized, and accelerated (left to right in Figure (1)) along the coaxial electrodes through a deflagration process[17,18]. The plasma subsequently assembles into a 50 cm long Z-pinch plasma column in the assembly region (Figure (1)). Continual gas injection and plasma acceleration along the coaxial electrodes results in radially-sheared, axial plasma flows acting to stabilize the Z-pinch against fast growing instabilities. Measured plasma lifetimes are 10 – 20 μs, or >1000 times greater than magnetohydrodynamic (MHD) instability growth times.

Previous results from FuZE[13] show pinch currents of >200 kA persisting for up to 15 μs, concurrent with measured ion densities and temperatures of 10^{17} cm^{-3} and $\sim$1 keV, respectively. With fill gas mixtures of 20 % D_2 in He, neutron yields and emission durations are $\sim 10^5$ neutrons per discharge and $\sim$5 μs, respectively. The neutron emitting region has a length of 33 cm (Figure (1)). The centroid of the neutron emitting region is located approximately 17 cm from the end of the cathode tip.

Previous work[13,14] used gas mixtures with different deuterium concentrations to show that all of the pulses observed during the neutron emission duration correspond to neutrons and not X-rays. This is an important conclusion, as the fast plastic scintillators used for measurements on FuZE are not capable of discriminating between X-rays and neutrons based on pulse-shape alone.

B. Energetically-resolved neutron measurements with plastic scintillator detectors

The procedure for fielding plastic scintillator detectors on the FuZE device is described previously[14]. The basic principles of fast neutron detection using organic scintillators are

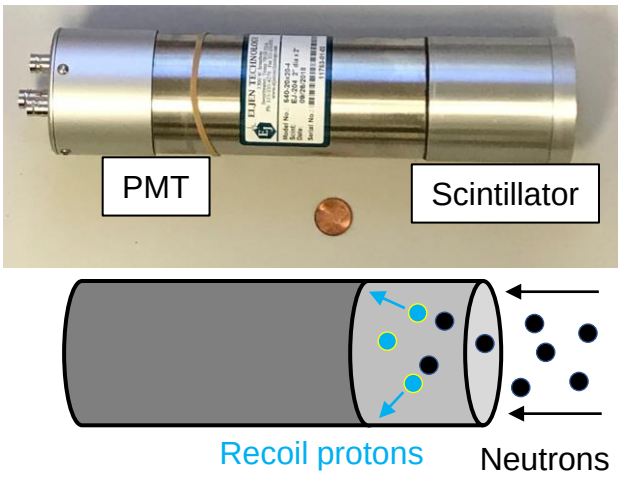

FIG. 2: (Top) Picture of one of the scintillator detectors used for neutron measurements on the FuZE device. (Bottom) Simplified schematic of the physical mechanism for pulse generation in the detector, where recoil protons produced by fast neutron interactions generate light via excitation and ionization of the scintillating medium. The scintillation light is converted to an electric signal using a photomultiplier tube (PMT).

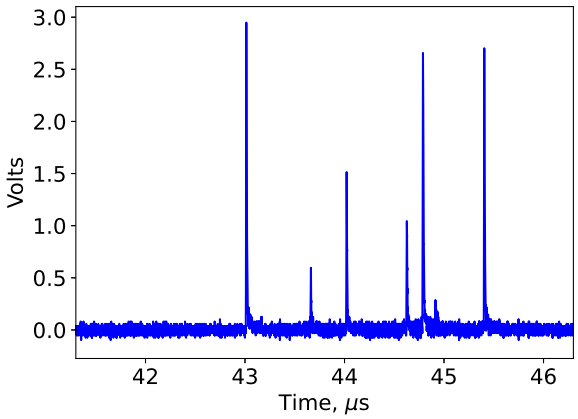

FIG. 3: Digitized trace from a FuZE discharge. The detector is operating in pulse-counting mode. Individual pulses correspond to light output from recoil protons in the plastic scintillator.

described in Klein and Brooks[19], and a picture of one of the scintillator detectors is shown in Figure (2). Neutron detectors consist of 5 cm length, 5 cm diameter, fast plastic scintillators (Eljen Technology, EJ-204, 0.7 ns rise time, and 1.8 ns decay time) that are coupled to fast PMTs (Hamamatsu R7724, 2.1 ns rise time). The PMT output is digitized using a 1 GHz bandwidth, deep-memory oscilloscope (Tektronix, DPO4104C). A characteristic waveform

from a FuZE discharge is shown in Figure (3).

The total light observed in an organic scintillator is related to the energy deposited by recoiling particles in the scintillator. For a given incident neutron energy, the distribution of recoiling particles can be modeled using the Geant4 toolkit[20]. The light generation from these recoil distributions is largely from proton energy deposition, which can be converted to light output using the measured non-linear relation between proton energy deposition and light production, the proton light yield. The conversion for this work was done using the EJ-204 proton light yield relation previously measured by Laplace *et al.*[21]. By using the proton light yield in conjunction with the detector resolution function[22], modeled neutron response functions can be generated for the detectors in a variety of neutron fields.

Neutron emission durations from FuZE are microseconds long (Figure (3)), which is significantly longer than neutron emission durations from inertial confinement fusion (ICF) plasmas (typically <1 ns) and significantly shorter than neutron emission durations from magnetic confinement fusion (MCF) plasmas (typically >1 ms). Consequently, neutron measurement techniques that are applied to ICF or MCF plasmas are not readily applicable to diagnosing neutron emission from FuZE. The neutron time-of-flight (nToF) method is commonly used to infer neutron energies from experiments with sub-microsecond neutron emission durations, such as laser-driven ICF experiments and dense Z-pinch experiments[23–25]. However, nToF measurements are difficult to apply on FuZE due to the microsecond long neutron emission durations. Magnetic recoil neutron spectrometers[26] are applied for absolute neutron energy measurements on the National Ignition Facility (NIF), but the efficiency of the magnetic recoil spectrometer is $\sim 10^{-9}$, which is too low to measure neutron emission on FuZE. Methods for measuring fusion neutron energies on MCF experiments, such as segmented spectrometers or ^{3}He spectrometers[27,28], often rely on neutrons thermalizing before interacting with a low-Z medium (e.g. ^{3}He, ^{6}Li). Consequently, the temporal responses of these methods are typically greater than 1 μs, which are too long with respect to neutron emission durations from the FuZE device.

Scintillation pulses were integrated using a functional form, $y(t)$, adapted from Friesen and Howell[29]:

$$y(t) = A_P[R_P(t) \cdot D_P(t) + r \cdot R_P(t + t_R) \cdot D_P(t + t_R)], \tag{2}$$

where A_P is the pulse amplitude, and $R_P(t)$ and $D_P(t)$ parametrize the pulse rise and decay,

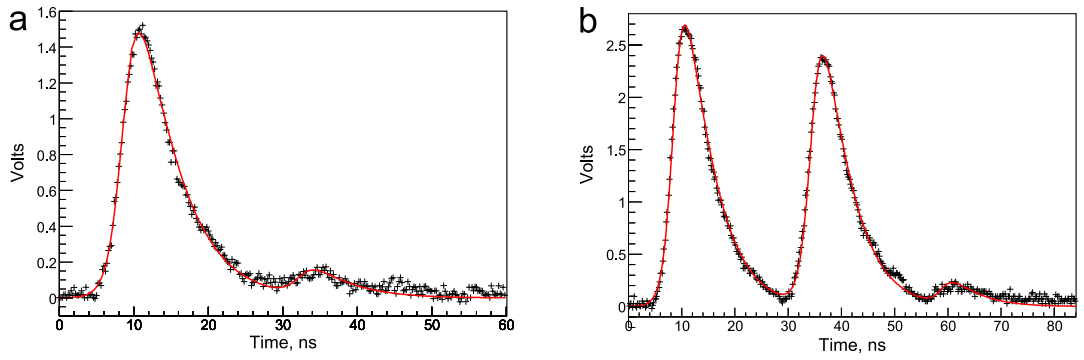

FIG. 4: (a) Example of fit for isolated scintillation pulse. (b) Example of successful fit for overlapping scintillation pulse.

respectively. A signal reflection was observed in the measured waveforms at time t_R from the scintillation pulse with relative amplitude r, accounting for the second term. The pulse rise, $R_P(t)$, is given by:

$$R_P(t) = \frac{1}{\exp\left(-\frac{t-t_0}{\tau_r}\right)+1}, \tag{3}$$

where t_0 is the pulse arrival time and τ_r is the rise time constant. Similarly, the pulse decay, $D_P(t)$, is given by:

$$D_P(t) = \frac{1}{\exp\left(\frac{t-t_0}{\tau_d}\right)+1}, \tag{4}$$

where τ_d is the decay time constant. Figure (4a) shows an example fit for an isolated scintillation pulse. Piled-up pulses (i.e., pulses that had not reached baseline before the start of the next pulse, which represented ∼19% of the events in the measured traces), were fit using parameters from isolated pulse fits as initial seeds. Figure (4b) shows an example of a successful fit of overlapping scintillation pulses. The goodness of fit was estimated by calculating the reduced chi-square, χ^2_ν, which can be defined as:

$$\chi^2_\nu = \frac{1}{N-m}\sum_i \left(\frac{y_i - f(x_i)}{\sigma_i}\right)^2. \tag{5}$$

When χ^2_ν is calculated for fits of scintillation pulses, y_i corresponds to the Volts for the measured pulses, $f(x_i)$ corresponds to the functional form (Equation (2)) of the fitted pulses, σ_i corresponds to the bit noise for the measured trace, N is the number of points used to fit the pulses, and m is the number of fit parameters. The distribution of χ^2_ν values is shown in

Figure (5). An arbitrary constraint was applied to discard fits with $\chi^2_\nu > 5$. This provided a recovery of 40% of piled-up pulses.

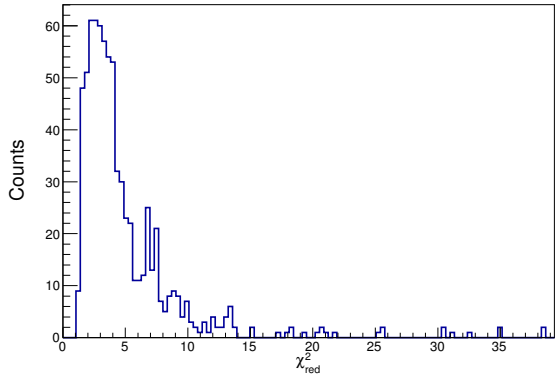

FIG. 5: Distribution of χ^2_ν for scintillation pulse fits.

III. THEORY

Measuring neutron energy emission profiles from fusing plasmas yields information about the origin of neutron production within the plasma. Neutron production from thermonuclear fusion reactions results in spatially isotropic neutron yield and energy profiles. Conversely, neutron production from non-thermal, beam-target fusion reactions results in strongly anisotropic neutron yield and energy emission profiles in the lab frame. Neutron energy emission profiles can be described by the following equation[30]:

$$E_n(\theta_B) = \frac{m_n}{2}\left(v_{cm}\cos\theta_B \pm \sqrt{\frac{m_4}{m_n(m_n+m_4)}(2Q + m_{ab}v_{ab}^2) - v_{cm}^2\sin^2\theta_B}\right), \tag{6}$$

where E_n is the emitted neutron energy as a function of the beam angle, θ_B; m_n, m_4, and m_{ab} are the neutron mass, helium-3 ion mass, and reduced mass of two deuterons, respectively; $Q = 3.27$ MeV is the net reaction energy of the DD fusion reaction; and v_{cm} and v_{ab} are the center-of-mass and relative velocities of two fusing deuterons, respectively. The term $m_{ab}v_{ab}^2 = E_d$ describes the energy of a mono-energetic deuteron beam incident on a thin, cold, stationary deuterium target. For deuteron beams with energies <100 keV, this term is much smaller than Q. However, because emitted neutron energies are dependent on the sum of the deuteron beam energy and the net reaction energy of the DD fusion

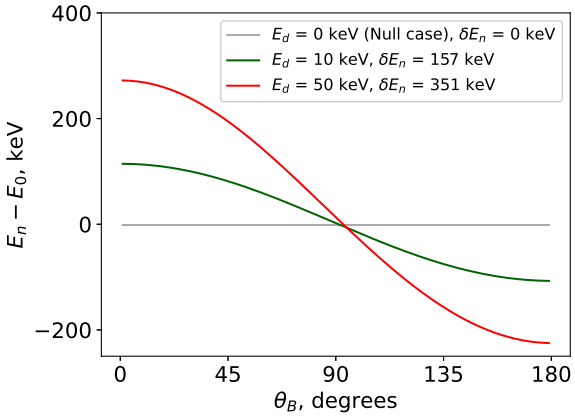

FIG. 6: Modeled neutron energies emission profiles (Eq. (6)) for mono-energetic deuteron beams with energies of $E_d = 0$, 10, and 50 keV. E_0 is equal to 2.45 MeV and δE_n refers to the difference between neutron energies emitted at a beam angle of 45° and neutron energies emitted at a beam angle of 135°. Note that δE_n is significantly larger than the deuteron beam energy.

reaction, the presence of deuteron beams with relatively low energies can cause relatively larger anisotropies in emitted neutron energies.

The magnitude of the anisotropy in emitted neutron energies is much larger than the actual deuteron beam energy. Figure (6) shows neutron energy emission profiles as a function of three deuteron beam energies, $E_d = \{0, 10, 50\}$ keV. The calculations in Figure (6) assume neutron emission from DD beam-target fusion reactions with mono-energetic deuteron beams and thin deuterium targets; here thin refers to the fact that deuterons are not slowed significantly in the plasma, which is true in this case. The null case ($E_d = 0$ keV) shows neutron energy emission is isotropic in the absence of a deuteron beam. A deuteron beam with an energy as low as $E_d = 10$ keV can cause significant anisotropies in emitted neutron energies, as the difference in neutron energies emitted at $\theta_B = 45°$ and $\theta_B = 135°$, or δE_n, is 157 keV. Larger deuteron beam energies of $E_d = 50$ keV will cause greater anisotropies in emitted neutron energies, as δE_n increases to 351 keV.

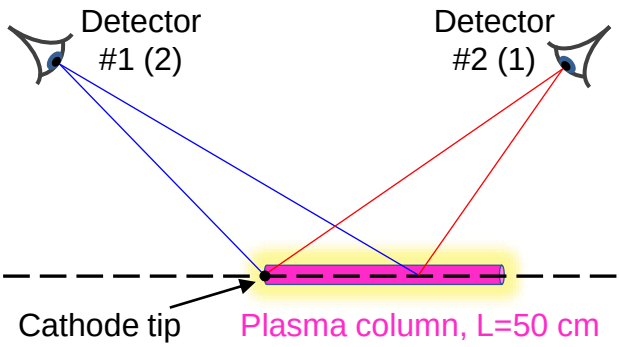

FIG. 7: Orientation of scintillator detectors with respect to fusing plasma. (The cathode, anode, and device chamber are not shown.) Scintillator detectors were placed upstream and downstream of the fusing plasma to detect neutron energy anisotropies from axial, beam-target fusion reactions.

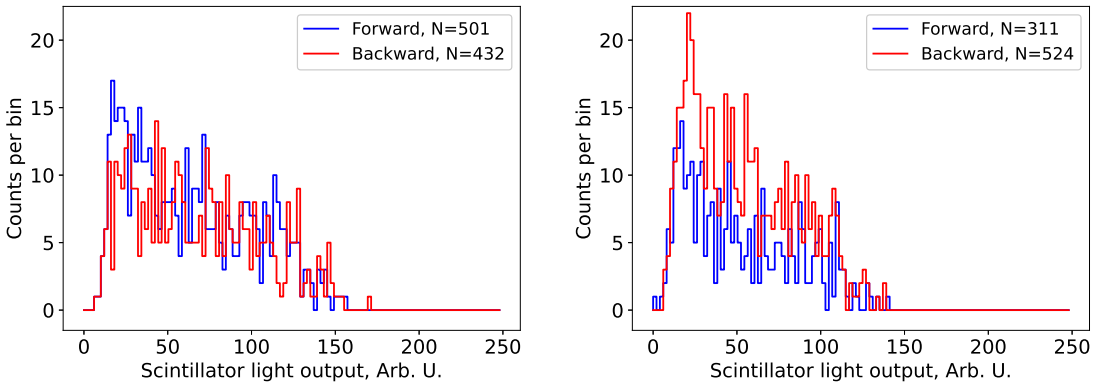

FIG. 8: Pulse integral spectra measured with detector #1 (left) and detector #2 (right) at two locations around the FuZE plasma column. In the figure legend, N refers to the total number of pulses in each spectrum. The scintillator light output corresponds to the integrated charge in arbitrary units.

IV. RESULTS

A. Measured pulse integral spectra

Figure (7) shows the relative locations of two scintillation detectors, denoted as detector #1 and detector #2, around the fusing plasma column. Measured pulse integral spectra for each detector at both detector locations are shown in Figure (8). For one set of 58

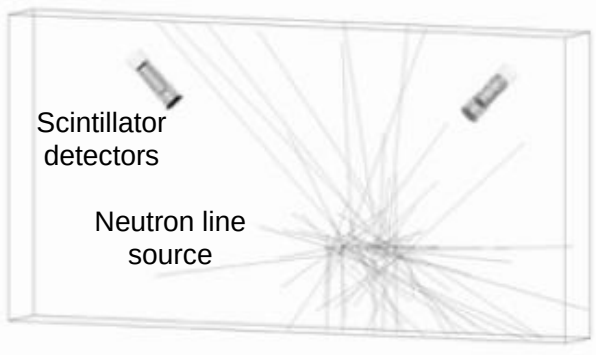

FIG. 9: Geometry showing locations of scintillator detectors with respect to a neutron line source in Geant4. Gray lines show simulated neutron tracks.

discharges, detector #1 was positioned at a location of (R, Z) = (45, 61) cm, and detector #2 was positioned at a location of (R, Z) = (45, -45) cm, where R and Z refer to radial and axial distances from the cathode tip, respectively. For a subsequent set of 58 discharges, the relative locations of the scintillation detectors were swapped. Detector #1 was moved to a location of (R, Z) = (45, -45) cm, and detector #2 was moved to a location of (R, Z) = (45, 61) cm. The absolute detector locations of (R, Z) = (45, -45) cm and (45, 61) cm were chosen to observe differences in measured spectra due to axial beam-target neutron production while minimizing artifacts of neutron attenuation and down-scattering from the FuZE chamber geometry.

A strong axial, deuteron beam traveling from the anode to the cathode (right to left, in Figures (1) and (7)) would cause an upshift in neutron energies incident on the left-most detector location, (R, Z) = (45, -45) cm, and a downshift in neutron energies incident on the right-most detector location, (R, Z) = (45, 61) cm.

B. Fits to pulse integral spectra

A novel, forward-fit method is applied to determine whether neutrons are emitted from thermonuclear or beam-target fusion reactions. This approach assumes that beam-target fusion reactions are driven by an axially propagating, mono-energetic deuteron beam with energy E_d. The forward-fit method is used to determine a value for E_d that results in a best fit between measured (Figure (8)) and simulated pulse integral spectra.

The forward fit requires a prediction of the observed spectra for each detector as a function

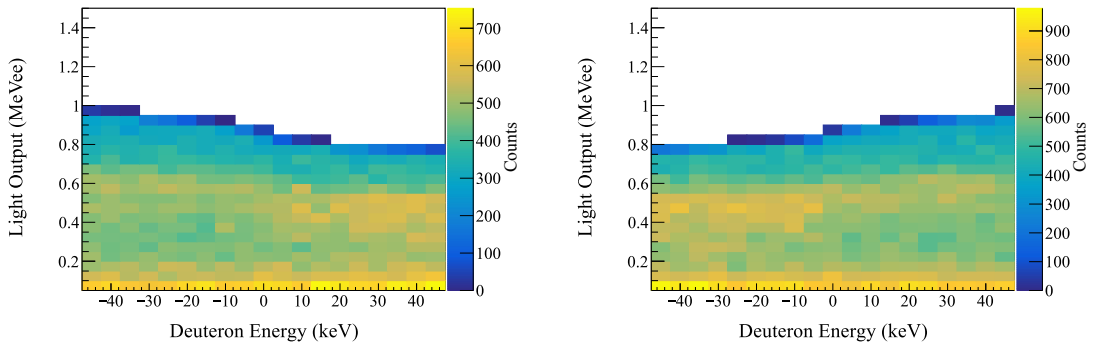

FIG. 10: Simulated scintillator light output as a function of deuteron beam energy, E_d. The two figures show the simulated pulse integral spectra for detector locations of (R, Z) = (45, -45) cm and (R, Z) = (45, 61) cm as a function of deuteron beam energy. Values of E_d varied from 0 (no beam present in plasma) to ±50 keV. For units used in this numerical calculation, negative values of E_d describe a deuteron beam propagating from the anode to cathode (right to left in Figure (7)).

of E_d. To accomplish this, the Geant4 toolkit is used to simulate neutrons incident on each of the scintillation detectors (Figure (9)) for a given E_d. The yield and energy emission profiles for a neutron line source are parametrized as a function of E_d. Equation (64) in Higginson *et al.*[30] is used to define a spatially-resolved neutron yield profile, and Equation (6) is used to define a spatially-resolved energy emission profile. The length of the neutron line source is 33 cm and is centered 16.5 cm from the cathode tip[14]. The characteristics of the neutron line source, locations of each scintillator detector, and materials surrounding the plastic scintillators (including the PMT, a thin aluminum case around the scintillator, and mu-metal around the PMT) are representative of experimental conditions (Figure (9)). Simulations were performed where the initial value of E_d for an event was sampled from a uniform distribution from -50 to 50 keV. Negative values of E_d describe a deuteron beam propagating from anode to cathode, or right to left in Figure (9), and in the opposite direction for positive values of E_d.

The energy deposited from recoiling protons in the scintillator as well as the initially sampled value of E_d were recorded on an event-by-event basis. Using the previously measured EJ-204 proton light yield relation from Laplace et al.[21], recoil proton energies were converted to relative scintillator light output. The units of relative light output are defined

with respect to the light that would be observed from an electron deposition of equivalent energy, or MeVee. A total of 1.2×10^{10} source particles were transported in the simulation. Figure (10) shows the results of accumulating the calculated light for each event into a two-dimensional histogram where the abscissa represents the initially selected deuteron energy, E_d; the ordinate axis represents the total light, L_ν, observed for a given event; and the z color bar represents the number of events observed per 0.05 MeVee per 5 keV E_d for 1.2×10^{10} simulated particles. These histograms represent the light observed by a detector with perfect light resolution and will be referred to as $\Lambda_j(E_d, L_\nu)$ where the jth subscript denotes the detector location index, i.e., $j = \{1, 2\}$. Detector locations of (R, Z) = (45, -45) cm and (R, Z) = (45, 61) cm are shown in Figure (7).

To calculate the likelihood that the observed data corresponds to a given E_d, projections of $\Lambda_j(E_d, L_\nu)$ are generated over E_d in 5 keV steps ranging from -50 to 50 keV yielding a series of light yield spectra, $\Lambda_j(L_\nu; E_d)$, for each 5-keV bin. The projections undergo several transformations to account for overall event normalization, the detector resolution, and the calibration from the measured integrated charge to the simulated MeVee relative light unit. The prediction of the measurement for the jth detector location, μ_j, is given by:

$$\mu_j(C; A, \alpha, \beta, \gamma, S_j, E_d) = R_\nu(C, \alpha, \beta, \gamma) * (S_j \times \Lambda_j(A \times C; E_d)) \,. \tag{7}$$

This introduces six parameters to the forward model: A, α, β, γ, S_1, and S_2. Here, $*$ is the convolution operator; A is an amplitude scalar used to convert the measured integrated charge, C, into MeVee; α, β, γ are parameters describing the amplitude dependent, detector resolution as a function of the integrated charge, $R_\nu(C, \alpha, \beta, \gamma)$ as described in Dietze and Klein[22]; and S_1, and S_2 represent normalization scalars.

The six parameters are determined by minimizing a loss function, defined as the negative log-likelihood, between the measured and simulated spectra. The log-likelihood assumes that measurement errors are independent and can be described by Poisson statistics. The loss function is defined as,

$$-\ln L = -\sum_{i,j} \ln \rho(y_{i,j}, \mu_{i,j}), \tag{8a}$$

$$= -\sum_{i,j} \ln \frac{\mu_{i,j}^{y_{i,j}} e^{\mu_{i,j}}}{y_{i,j}!}, \tag{8b}$$

where ρ is a Poisson distribution, i is the bin index, j is the detector location index, $y_{i,j}$ is the number of counts in the ith bin of the measured spectrum of the jth detector position,

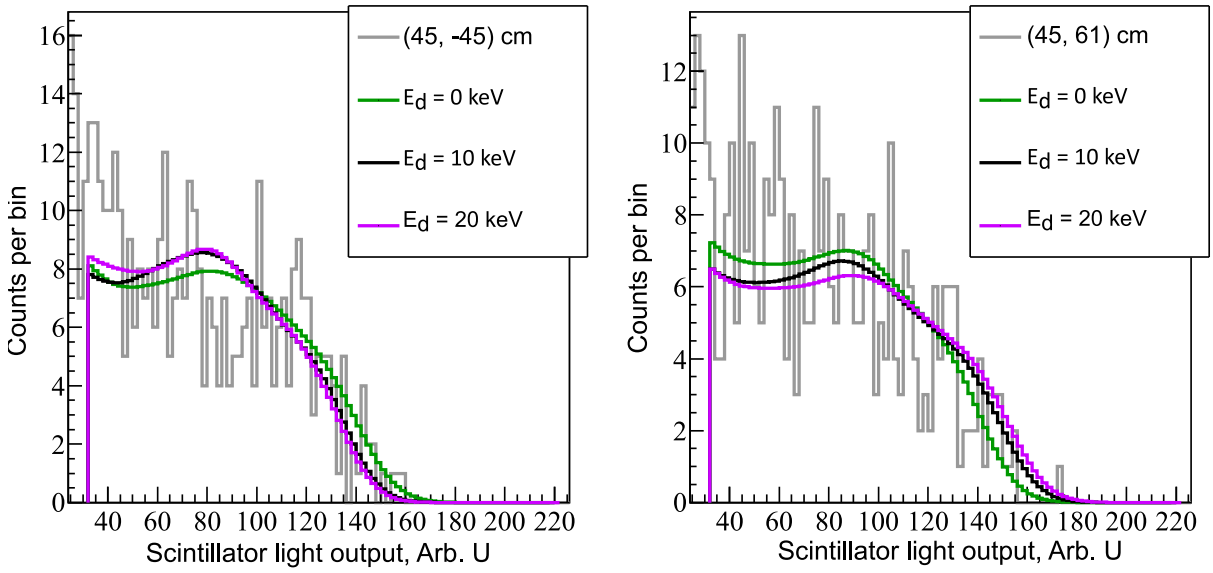

FIG. 11: Illustrative plot showing measured and simulated spectra for detector #1, for scintillator detector locations of (R, Z) = (45, -45) cm (left) and (R, Z) = (45, 61) cm (right). In the plots above, simulated spectra are calculated for fixed values of E_d = 0, 10, 20 keV.

and $\mu_{i,j}$ is the predicted counts for the ith bin of the simulated spectrum for detector location j given by Equation (7). The minus sign in front of $-\ln L$ is used so that best-fit values of fit parameters in μ can be calculated with an existing numerical minimizer[31]. Therefore, the loss (Equation (8)) is minimized for all parameters of μ for each E_d in the range.

For illustrative purposes, Figure (11) shows simulated spectra overlaid with measured spectra for detector #1 at both detector locations. Values of E_d = 0, 10, and 20 keV are used for calculating the simulated spectra. Each spectrum is transformed by the six parameters, A, α, β, γ, S_1, and S_2, as described previously (Equation (7)). Values of the six parameters are determined for each of the three simulated spectra in Figure (11) by minimizing the loss function (Equation (8)) between the measured and simulated spectra. Values calculated by the loss function between the measured and simulated pulse integral spectra are 61.4 for E_d = 0 keV, 64.1 for E_d = 10 keV, and 68.6 for E_d = 20 keV. These values between the measured and simulated spectra are calculated over a range of values of 0.2 – 1.3 MeVee (Figure (10)). A total of 125 bins was used for constructing the measured and simulated spectra in Figure (11)

The best fit of E_d is determined by calculating the loss (Equation (8)) over the full grid

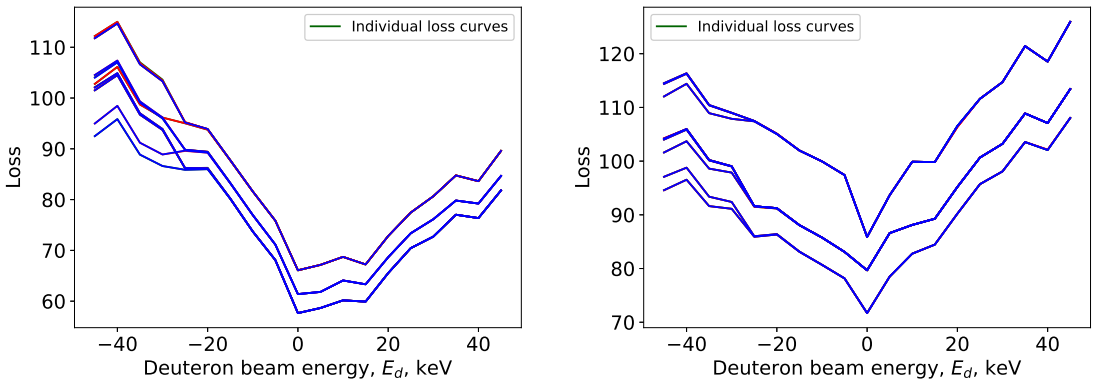

FIG. 12: Results of scanning over user-specified parameters for detectors #1 (left) and #2 (right). Each individual loss curve is calculated with different values for the set of user-specified parameters of the forward-fit model. The loss corresponds to negative log-likelihood values, as defined in Equation (8).

of values of E_d in Figure (10). A 2nd degree polynomial function,

$$L_{Fit} = A_0 + A_1 \times E_d + A_2 \times E_d^2, \tag{9}$$

is fitted to the loss calculated as a function of E_d. The best fit value of E_d is found at the minimum of the fitted polynomial curve, $E_d^* = -0.5A_1/A_2$. The statistical uncertainty[32] corresponds to the intercept between the loss curve and loss values equal to $L_{min} + 0.5$, where L_{min} is the value of the fitted polynomial calculated at E_d^*.

The systematic uncertainty of E_d is determined by scanning over user-specified parameters of the forward-fit method. User-specified parameters include: initial conditions for the minimizer, the fit range, and the number of bins in each spectrum. The initial conditions for the minimizer correspond to projections of the simulated spectra onto the measured spectra for a fixed value of E_d. Values of E_d equal to 0, +25 keV, and -25 keV were used to generate each of the three initial conditions for the minimizer. The fit range corresponds to the range of recoil proton energies over which the measured and simulated spectra are compared. The lower and upper values for the fit range varied from 0.17 – 0.23 MeVee and 1.2 – 1.4 MeVee, respectively. Constructing spectra with 55, 75, 105, or 125 bins has no statistically significant effect on the inferred value or uncertainty of E_d. The number of bins was chosen to resolve the edge of the spectra. Varying the initial conditions of the minimizer, fit range, or number of bins has no statistically significant impact on the inferred value of E_d.

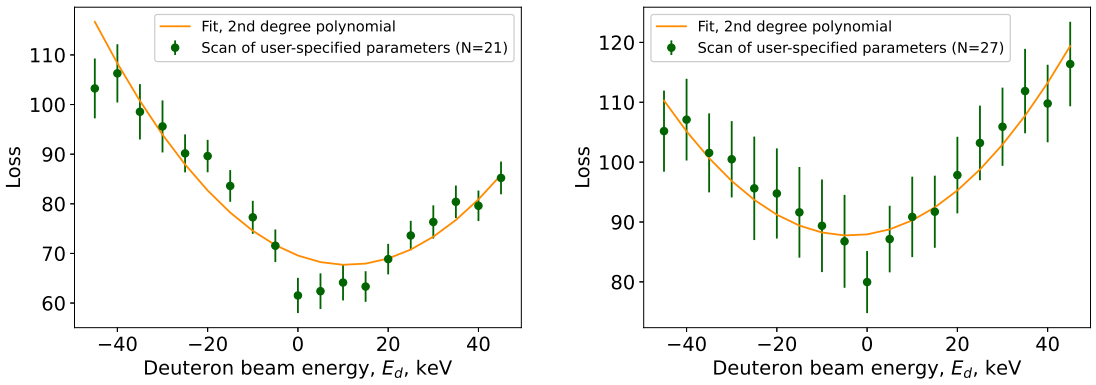

FIG. 13: Results for 2nd degree polynomial fits (orange curve) to loss curves (green points) for detectors #1 (left) and #2 (right). For detector #1, the fitted value of E_d^* is 10.96 keV, with a statistical uncertainty of 5.65 keV and a systematic uncertainty of 0.60 keV. For detector #2, the fitted value of E_d^* is -3.81 keV, with statistical and systematic uncertainties of 6.13 and 1.11 keV, respectively. The loss corresponds to negative log-likelihood values, as defined in Equation (8).

	Detector #1	Detector #2
E_d^*	10.96	-3.81
Statistical uncertainty	5.65	6.13
Systematic uncertainty	0.60	1.11

TABLE I: Results from fits to data in Figure (13). Values for $\mathrm{A}_i (i = 0, 1, 2)$ correspond to fit parameters in a 2nd degree polynomial function and E_d^* corresponds to the value of E_d that best fits the data. Values and uncertainties of E_d^* are in units of keV.

Figures (12) and (13) show results from scanning over user-specified parameters. Figure (12) shows individual loss curves calculated for each detector as a function of E_d. Values for the loss shown in Figures (12) and (13) correspond to negative log-likelihood values (Equation (8)). The individual loss curves (Figure (12)) are calculated with different values of user-specified parameters, including the fit range and initial conditions for the minimizer. For example, one of the loss curves in Figure (12) is calculated with a fit range of 0.17 – 1.3 MeVee and one set of initial conditions. A different loss curve in Figure (12) is calculated with a fit range of 0.2 – 1.4 MeVee and a different set of initial conditions. The number of

bins in the measured and simulated spectra for each of the individual loss curves in Figure (12) is fixed at 125. Individual loss curves with the same number of bins can be averaged to calculate an average loss curve as a function of E_d.

Figure (13) shows average loss curves for each detector. The green data points in Figure (13) correspond to the mean and standard deviation of individual loss curves in Figure (12). Chi-square minimization (Equation 5) is used to fit a 2nd degree polynomial curve, $L_{Fit}(E_{d,i})$ (Equation 9), to the data points. Values of y_i and σ_i correspond to the mean and standard deviation of the loss curves. Fit results are shown in Table (I). For detector #1, the value of E_d that best fits the data, E_d^*, is 10.96 keV with a statistical uncertainty of 5.65 keV and a systematic uncertainty of 0.60 keV. For detector #2, E_d^* has a value of -3.8 keV with a statistical uncertainty of 6.13 keV and a systematic uncertainty of 1.11 keV. The systematic uncertainty of E_d^* is found from the uncertainty of the fit parameters, A_i. The uncertainty of the fit parameters is determined by calculating the covariance matrix of the fit. The formula used to calculate the systematic uncertainty is,

$$U_{Sys} = \mid 0.5E_d^* \mid \times \sqrt{\left(\frac{\sigma_{A_1}}{A_1}\right)^2 + \left(\frac{\sigma_{A_2}}{A_2}\right)^2 - \frac{\sigma_{A_1,A_2}}{A_1 A_2}}, \tag{10}$$

where U_{Sys} is the systematic uncertainty, σ_{A_i} is the uncertainty in the fit parameter $A_i (i = 1, 2)$, and σ_{A_1,A_2} is the covariance between A_1 and A_2. Using inverse-variance weighting, the weighted average of E_d^* is 4.65 keV, with an average statistical uncertainty of 4.15 keV and an average systematic uncertainty of 0.53 keV.

V. DISCUSSION

The results shown in Figure (13) and Table (I) facilitate determination of the primary mechanism for neutron emission from FuZE (i.e., beam-target fusion vs. thermonuclear). Based on the measured pulse integral spectra from detectors #1 and #2, the results indicate the presence of a 4.65 keV ± 4.15 keV ± 0.53 keV deuteron beam propagating from the cathode to the anode. Based on electrode polarity, beam-target fusion reactions are typically driven by an energetic deuteron beam propagating from the anode to cathode[33]. In Z-pinch plasmas, beam-target fusion reactions are typically caused by m=0 "sausage" instabilities, which creates large, transient electric-fields. The electric-fields will drive energetic deuteron beams into a deuterium target[15,16], resulting in neutron production through beam-target

fusion reactions. Previous measurements from dense Z-pinch devices have observed production of deuteron beams with energies in excess of 100 keV[34–36]. Given that neutron energy emission from the FuZE device has not shown significant energy anisotropies, thermonuclear fusion reactions are likely to be the dominant source of neutron production.

Note that the FuZE device generates radially-sheared, axial plasma flows along the pinch axis. Axial flow velocities of ∼120 km/s have been inferred from measurements on the FuZE device[17], which would correspond to a mono-energetic, deuteron beam energy of ∼0.15 keV. The direction and low energy ($\ll$ 100 keV) of the inferred deuteron beam is consistent with thermonuclear neutron emission from a quiescent plasma in the FuZE device.

Future work will involve fielding additional scintillation detectors around the FuZE device chamber to rule out non-thermal neutron emission from a greater range of instabilities and increase measurement statistics. The results in Figure (13) and Table (I) were obtained by measuring relative neutron energies at two detector locations (Figure (7)) around the fusing plasma. With two detector locations, the presence of energetic, axial deuteron beams from m=0 instabilities can be precluded. Non-thermal neutron production driven by m=0 instabilities is the dominant source of neutron emission from several dense Z-pinch devices. Observing isotropic neutron energy emission at more detector locations can preclude the presence of non-thermal fusion reactions from other types of plasma instabilities.

Fielding more scintillator detectors around the FuZE device chamber will also allow for increased measurement statistics over fewer discharges. The pulse integral spectra shown in Figure (8) were integrated over 58 discharges per spectra. The average number of pulses measured for an individual discharge on a single detector must be kept small in order to minimize the effects of pulse pileup. Neutron emission durations from the FuZE device are $\sim 2 - 5$ μs. The functional form (Equation (2)) used for pulse integrals was fitted over a 56 ns integration pathlength. Fielding multiple detectors at each detector location would allow for pulse integral spectra with more statistics and/or pulse integral spectra constructed over fewer discharges.

Future work will also include inferring absolute neutron energies from pulse integral spectra constructed using calibrated detectors. Plastic scintillator detectors can be calibrated by measuring Compton spectra from gamma sources with known emission energies, such as ^{137}Cs or ^{60}Co. Photons emitted from gamma sources undergo Compton scattering with electrons in the scintillator. The resulting scintillator light output spectrum can be used

to determine parameters for detector resolution and provide a reference standard for the scintillator light output. Light output units for recoil proton energies can then be expressed in units relative to the light output associated with a given electron energy (e.g., Compton edge of a ^{137}Cs spectrum). Using a measured Compton spectrum from a gamma source to calibrate scintillator light output units along with the measured proton light yield relations could also enable absolute neutron energy measurements with a single scintillator detector. Additionally, the three parameters (α, β, γ in Equation (7)) that define detector resolution can be derived from a calibration with a gamma source. Because the scintillator detectors used in the present work were not calibrated, the three parameters were treated as free parameters.

VI. CONCLUSION

Results presented in this manuscript preclude the possibility of axial, beam-target fusion reactions as the dominant source of neutron emission from the FuZE device. Together with long neutron emission durations[13], these results indicate thermonuclear neutron production from FuZE, which is a necessary condition for scaling the FuZE device up to fusion reactor conditions. Future work will involve refining the measurement technique to monitor for anisotropies in emitted neutron energies as SFS Z-pinch devices operate with greater device powers and higher pinch currents.

VII. ACKNOWLEDGMENTS

The authors would like to thank Bob Geer and Daniel Behne for technical assistance, as well as Amanda Youmans, Christopher Cooper, Clément Goyon for advice and discussions. The authors would also like to thank Phil Kerr and Vladimir Mozin for the use of their Thermo Fisher P385 neutron generator, which was important in verifying the ability to measure neutron energy shifts via the pulse integral technique. The information, data, or work presented herein was funded in part by the Advanced Research Projects Agency - Energy (ARPA-E), U.S. Department of Energy, under Award Numbers DE-AR-0000571, 18/CJ000/05/05, and DE-AR-0001160. This work was performed under the auspices of the U.S. Department of Energy by Lawrence Livermore National Laboratory under Contract DE-

AC52-07NA27344 and Lawrence Berkeley National Laboratory under Contract DE-AC02-05CH11231. U. Shumlak gratefully acknowledges support of the Erna and Jakob Michael Visiting Professorship at the Weizmann Institute of Science and as a Faculty Scholar at the Lawrence Livermore National Laboratory.

VIII. DATA AVAILABILITY

The data that support the findings of this study are available from the corresponding author upon reasonable request.

REFERENCES

[1]Lawson, John D, "Some criteria for a power producing thermonuclear reactor," Proceedings of the physical society. Section B **70**, 6 (1957).

[2]Shumlak, Uri and Nelson, BA and Claveau, EL and Forbes, EG and Golingo, RP and Hughes, MC and Oberto, RJ and Ross, MP and Weber, TR, "Increasing plasma parameters using sheared flow stabilization of a Z-pinch," Physics of Plasmas **24**, 055702 (2017).

[3]U. Shumlak, "Z-pinch fusion," Journal of Applied Physics **127**, 200901 (2020).

[4]W. H. Bennett, "Magnetically self-focussing streams," Physical Review **45**, 890 (1934).

[5]M. Haines, "A review of the dense z-pinch," Plasma Physics and Controlled Fusion **53**, 093001 (2011).

[6]M. D. Kruskal and M. Schwarzschild, "Some instabilities of a completely ionized plasma," Proceedings of the Royal Society of London. Series A. Mathematical and Physical Sciences **223**, 348–360 (1954).

[7]I. Kurchatov, "On the possibility of producing thermonuclear reactions in a gas discharge," Journal of Nuclear Energy (1954) **4**, 193–202 (1957).

[8]R. Carruthers and P. Davenport, "Observations of the instability of constricted gaseous discharges," Proceedings of the Physical Society. Section B **70**, 49 (1957).

[9]Shumlak, U and Hartman, CW, "Sheared flow stabilization of the m= 1 kink mode in Z pinches," Physical review letters **75**, 3285 (1995).

[10]Shumlak, U and Golingo, RP and Nelson, BA and Den Hartog, DJ, "Evidence of stabilization in the Z-pinch," Physical review letters **87**, 205005 (2001).

[11]Kadomtsev, BB, "Hydromagnetic stability of a plasma," Reviews of plasma physics **2**, 153–199 (1966).

[12]Shumlak, U and Adams, CS and Blakely, JM and Chan, B-J and Golingo, RP and Knecht, SD and Nelson, BA and Oberto, RJ and Sybouts, MR and Vogman, GV, "Equilibrium, flow shear and stability measurements in the Z-pinch," Nuclear Fusion **49**, 075039 (2009).

[13]Zhang, Y and Shumlak, U and Nelson, BA and Golingo, RP and Weber, TR and Stepanov, AD and Claveau, EL and Forbes, EG and Draper, ZT and Mitrani, JM and McLean, HS and Tummel, KK and Higginson, DP and Cooper, CM, "Sustained Neutron Production from a Sheared-Flow Stabilized Z Pinch," Physical Review Letters **122**, 135001 (2019).

[14]J. M. Mitrani, D. P. Higginson, Z. T. Draper, J. Morrell, L. A. Bernstein, E. L. Claveau, C. M. Cooper, E. G. Forbes, R. P. Golingo, B. A. Nelson, *et al.*, "Measurements of temporally-and spatially-resolved neutron production in a sheared-flow stabilized Z-pinch," Nuclear Instruments and Methods in Physics Research Section A: Accelerators, Spectrometers, Detectors and Associated Equipment **947**, 162764 (2019).

[15]Krishnan, Mahadevan, "The dense plasma focus: A versatile dense pinch for diverse applications," IEEE Transactions on Plasma Science **40**, 3189–3221 (2012).

[16]M. G. Haines, "Ion beam formation in an m= 0 unstable z pinch," Nuclear Instruments and Methods in Physics Research **207**, 179–185 (1983).

[17]A. Stepanov, U. Shumlak, H. McLean, B. Nelson, E. Claveau, E. Forbes, T. Weber, and Y. Zhang, "Flow Z-pinch plasma production on the FuZE experiment," Physics of Plasmas **27**, 112503 (2020).

[18]Golingo, Raymond Peter and Shumlak, U and Nelson, BA, "Formation of a sheared flow Z pinch," Physics of Plasmas **12**, 062505 (2005).

[19]H. Klein and F. D. Brooks, "SCINTILLATION DETECTORS FOR FAST NEUTRONS ," in *Proceedings of International Workshop on Fast Neutron Detectors and Applications — PoS(FNDA2006)*, Vol. 025 (2007) p. 097.

[20]S. Agostinelli, J. Allison, K. Amako, J. Apostolakis, H. Araujo, P. Arce, M. Asai, D. Axen, S. Banerjee, G. Barrand, *et al.*, "Geant4—a simulation toolkit," Nuclear Instruments and Methods in Physics Research Section A: Accelerators, Spectrometers, Detectors and Associated Equipment **506**, 250–303 (2003).

[21]T. Laplace, B. Goldblum, J. A. Brown, D. Bleuel, C. Brand, G. Gabella, T. Jordan, C. Moore, N. Munshi, Z. Sweger, *et al.*, "Low energy light yield of fast plastic scintil-

lators," Nuclear Instruments and Methods in Physics Research Section A: Accelerators, Spectrometers, Detectors and Associated Equipment **954**, 161444 (2020).

[22]G. Dietze and H. Klein, "Gamma-calibration of "NE" 213 scintillation counters," Nuclear Instruments and Methods in Physics Research **193**, 549–556 (1982).

[23]V. Y. Glebov, C. Forrest, J. Knauer, A. Pruyne, M. Romanofsky, T. Sangster, M. Shoup III, C. Stoeckl, J. Caggiano, M. Carman, *et al.*, "Testing a new NIF neutron time-of-flight detector with a bibenzyl scintillator on OMEGA," Review of Scientific Instruments **83**, 10D309 (2012).

[24]V. Y. Glebov, C. Stoeckl, T. Sangster, S. Roberts, G. Schmid, R. Lerche, and M. Moran, "Prototypes of National Ignition Facility neutron time-of-flight detectors tested on OMEGA," Review of scientific instruments **75**, 3559–3562 (2004).

[25]Gomez, Matthew R and Slutz, Stephen A and Sefkow, Adam B and Sinars, Daniel B and Hahn, Kelly D and Hansen, Stephanie B and Harding, Eric C and Knapp, Patrick F and Schmit, Paul F and Jennings, Christopher A and others, "Experimental demonstration of fusion-relevant conditions in magnetized liner inertial fusion," Physical review letters **113**, 155003 (2014).

[26]D. Casey, J. Frenje, M. Gatu Johnson, F. Séguin, C. Li, R. Petrasso, V. Y. Glebov, J. Katz, J. Magoon, D. Meyerhofer, *et al.*, "The magnetic recoil spectrometer for measurements of the absolute neutron spectrum at OMEGA and the NIF," Review of Scientific Instruments **84**, 056311 (2013).

[27]Langford, TJ and Bass, CD and Beise, EJ and Breuer, H and Erwin, DK and Heimbach, CR and Nico, JS, "Fast neutron detection with a segmented spectrometer," Nuclear Instruments and Methods in Physics Research Section A: Accelerators, Spectrometers, Detectors and Associated Equipment **771**, 78–87 (2015).

[28]Czirr, J Bart and Jensen, Gary L, "A compact neutron coincidence spectrometer, its measured response functions and potential applications," Nuclear Instruments and Methods in Physics Research Section A: Accelerators, Spectrometers, Detectors and Associated Equipment **349**, 532–539 (1994).

[29]F. Friesen and C. Howell, "A functional form for liquid scintillator pulse shapes," Nuclear Instruments and Methods in Physics Research Section A: Accelerators, Spectrometers, Detectors and Associated Equipment **955**, 163302 (2020).

[30]D. P. Higginson, A. Link, and A. Schmidt, "A pairwise nuclear fusion algorithm for weighted particle-in-cell plasma simulations," Journal of Computational Physics **388**, 439–453 (2019).

[31]R. Brun and F. Rademakers, "Root — an object oriented data analysis framework," Nuclear Instruments and Methods in Physics Research Section A: Accelerators, Spectrometers, Detectors and Associated Equipment **389**, 81–86 (1997), new Computing Techniques in Physics Research V.

[32]F. Porter, "Interval estimation using the likelihood function," Nuclear Instruments and Methods in Physics Research Section A: Accelerators, Spectrometers, Detectors and Associated Equipment **368**, 793–803 (1996).

[33]S. Jiang, D. Higginson, A. Link, I. Holod, and A. Schmidt, "Effect of polarity on beam and plasma target formation in a dense plasma focus," Physics of Plasmas **26**, 042702 (2019).

[34]J. Linhart, "Beam-target fusion in a dense z-pinch," Plasma physics and controlled fusion **30**, 1641 (1988).

[35]W. Stygar, G. Gerdin, F. Venneri, and J. Mandrekas, "Particle beams generated by a 6–12.5 kJ dense plasma focus," Nuclear Fusion **22**, 1161 (1982).

[36]H. Krompholz, L. Michel, K. Schoenbach, and H. Fischer, "Neutron-, ion-, and electron-energy spectra in a 1 kJ plasma focus," Applied physics **13**, 29–35 (1977).